

Fraction of clear skies above astronomical sites: a new analysis from the GOES12 satellite

S. Cavazzani^{1*}, S. Ortolani¹, V. Zitelli², Y. Maruccia³

¹*Department of Astronomy, University of Padova, Vicolo dell'Osservatorio 3, I-35122, Padova, Italy*

²*INAF-Osservatorio Astronomico di Bologna, via Ranzani 1, I-40127, Bologna, Italy*

³*Department of Physics, University of Salento, Via per Arnesano, CP 193, 73100 Lecce, Italy*

Accepted 2010 September 24. Received 2010 September 24; in original form 2010 May 25.

ABSTRACT

Comparing the number of clear nights (cloud free) available for astronomical observations is a critical task because it should be based on homogeneous methodologies. Current data are mainly based on different judgements based on observer logbooks or on different instruments. In this paper we present a new homogeneous methodology on very different astronomical sites for modern optical astronomy, in order to quantify the available night time fraction. The data are extracted from night time GOES12 satellite infrared images and compared with ground based conditions when available. In this analysis we introduce a wider average matrix and 3-Bands correlation in order to reduce the noise and to distinguish between clear and stable nights. Temporal data are used for the classification. In the time interval 2007-2008 we found that the percentage of the satellite clear nights is 88% at Paranal, 76% at La Silla, 72.5% at La Palma, 59% at Mt. Graham and 86.5% at Tolonchar. The correlation analysis of the three GOES12 infrared bands B3, B4 and B6 indicates that the fraction of the stable nights is lower by 2% to 20% depending on the site.

Key words: atmospheric effects – site testing – methods: statistical.

1 INTRODUCTION

The efficiency of the astronomical telescopes is critically dependent on the cloud coverage. The knowledge of the clear night time fraction is then fundamental for the choice of a telescope site, and, on already existing facilities, its distribution during the year, as well as long term trends, are very important for planning the observations and the development of the instrumentation. In the last century the quantification of the night time clear fraction was based mainly on specific visual inspection of the sky conditions or on the observational logbooks of the telescopes. These methods are "internally" robust, but they are dependent on the experience of the observer and on the quality of the site. In short time tests there could be also some dependence on the Moon phase. An adequate time coverage is time consuming and expensive when applied to several, new sites. The use of the archives of satellite images allows, instead, to investigate simultaneously several sites in a time base of several years. In this study night time satellite derived parameters are used to assess the clear-usable fraction from the Geostationary Operational Environmental Satellite 12 (GOES12) archive.

The selected sites are chosen in order to test different climatic conditions and are located in Chile, USA and Spain (Canary Islands), (See Fig. 1).

Most of them are already well known, developed sites and host large, modern telescopes. The site of Tolonchar, instead, have been studied during the Thirty Meter Telescope (TMT) survey, but it is located in relatively little known area for the optical near-infrared astronomy. In this analysis we have a double goal: to check the reliability of our analysis method, to explore the characteristics of new regions and to compare them. The GOES satellite data have been studied with the goal to study environmental conditions, but they have been recently used also for the study of cloud coverage and water vapor content above some astronomical sites (Erasmus & van Rooyen (2006), della Valle et al. (2010) (PaperIII)). The advantage of GOES over other satellites is to have a very stable and very high orbit, allowing the collection of simultaneous images of almost half of the Earth hemisphere, still with a high resolution (4 km in the infrared (IR)). In this way site to site random biases, due to instrument instabilities are reduced. Furthermore the infrared channels allow the detection of the thermal radiation emitted during the night from different atmospheric layers and/or from the soil. An appropriate choice of the wave-

* E-mail: stefano.cavazzani@unipd.it

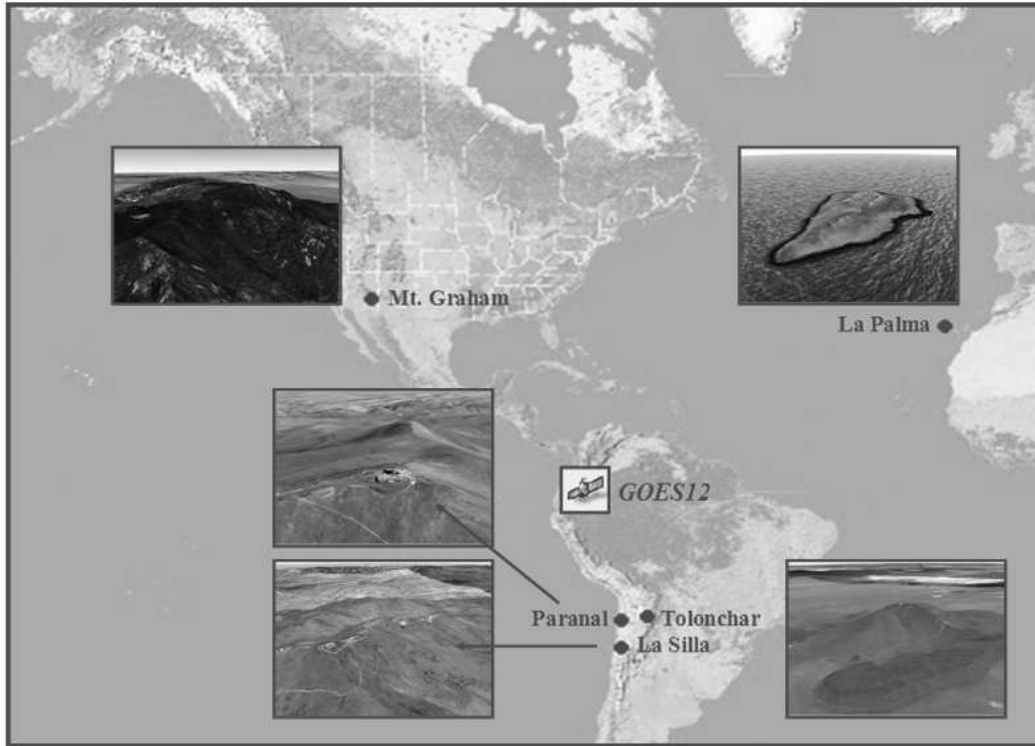


Figure 1. Location of the five sites involved in the analysis. As seen in the inserts the selected sites presents very different topographic conditions: La Palma is a sharp island, Mt. Graham a relatively wide plateau, Paranal, Tolonchar and La Silla are isolated peaks over a desertic altiplano. The position of GOES12 satellite projected on the map.

length allows to choose the optimal layer emission height above the site. If it occurs well above the soil surface, the signal becomes independent of the specific soil properties and of low level conditions. Phenomena occurring below the selected site (fog, low clouds...) are also avoided. In some sites, for example at La Palma, this aspect is of crucial importance. The channels used in our analysis have been selected with the above discussed criteria and are summarized in Table 1. In a previous paper (Paper III) we studied the clear sky fraction at La Palma and Mt. Graham, from ground and satellite, using an approach similar to Erasmus & van Rooyen (2006), but we have used direct GOES12 satellite brightness temperature measurements. In this paper the descriptions of the adopted definitions used to classify the nights are reported in Sections 7.1.2 and 7.1.3. The new adopted method is validated using the database of La Palma and Paranal and, after the positive results, it is applied to the other sites under investigation. The paper is organized as follows:

- in Section 2 we describe the used database,
- in Section 3 we describe the satellite data acquisition procedure,
- in Section 4 we describe the mathematical used model,
- in Section 5 we describe the IR analysis,
- in Section 6 we describe the atmospheric correlation function,
- in Section 7 we report the data analysis and discussion of the results.

Table 1. GOES12 bands and resolution at Nadir.

	Window	Passband [μm]	Resolution [km]
<i>BAND1</i>	Visible	$0,55 \div 0,75$	4
<i>BAND2</i>	Microwaves	$3,80 \div 4,00$	4
<i>BAND3</i>	H_2O	$6,50 \div 7,00$	4
<i>BAND4</i>	IR	$10,20 \div 11,20$	4
<i>BAND6</i>	CO_2	13.30	8

2 THE USED DATABASE

In this analysis we have used several sets of data collected from ground and satellite facilities partially available via web and partially obtained thanks to the courtesy of the observatory staff. The validation of satellite data are also performed via correlations among ground based and satellite data. In this paper we have sampled the years 2007 and 2008. Table 2 shows the characteristics of the used databases.

2.1 Ground Based Data

Differences at La Palma microclimate have been discussed in previous papers (Lombardi et al. (2006) (hereafter Paper I), Lombardi et al. (2007) (hereafter Paper II), and della Valle et al.(2010) (Paper III)). Paper I shows a complete analysis of the vertical temperature gradients and their correlation with the astronomical seeing, Paper II shows an analysis of the correlation between wind and astronomical parameters as well as the overall long term weather conditions at La

Palma. A statistical fraction of clear nights from satellite has been derived in Paper III using a basic approach to test the ability of the satellite to select clear nights. In order to have a reference for a classification of the nights at La Palma we used three different sources: the logbooks obtained from TNG (Telescopio Nazionale Galileo) and from the Liverpool telescope, and the data from the TNG meteorological station. The logbooks have been used merging the information, filling the gaps and checking the comments in case of contradictory classifications. The data from TNG meteorological station have been used to understand the status of ambiguous or unclassified nights in terms of humidity or wind speed limits. In general the agreement was good, but in winter time all the three sources were often needed in order to have a realistic view of the night weather evolution. The study of the telescope logbooks at Paranal was not needed because the night status data are obtained from the web pages of the ESO (European Southern Observatory) Observatories Ambient Conditions Database¹. They are very detailed pages containing the hourly humidity, temperature, atmospheric pressure, direction and wind speed. In addition there are measures of seeing through the DIMM (Differential Image Motion Monitor) and measures of the flux of a reference star. In particular the flux can trace the presence of clouds. The same website is also available for La Silla, but unfortunately in this case the web page is less detailed and often the data are missing. La Silla database is used as a further check. Both the sites of La Palma and Paranal are used to test and validate the new model applied in this paper.

2.2 Satellite Based Data

In these last decades the site testing have been conducted adding to the traditional meteorological instruments the use of the satellite data. Satellite archives contain several parameters useful for astronomical observations, allowing to compare different sites in a suitable way. Varela et al. (2008) give an exhaustive presentation of the satellites used for site testing. In our analysis we have chosen among the other available satellites the GOES satellite because it detects the IR night time emitted radiation. A detailed discussion is presented in Sec. 2.2.1. GOES is an American geosynchronous weather facilities of the National Oceanic and Atmospheric Administration (NOAA), and it is able to observe the full Earth disk. It is designed to detect surface temperature and the cloud cover, in addition to other important meteorological parameters. GOES12 have on board an imager covering five wavelength channels, one in the visible bands and four in the infrared bands (see Table 1). The maximum temporal resolution of the full Earth-disk scans is 41 sec that is a very high temporal sampling. Moreover GOES have also a high spatial resolution. It should be noticed that GOES12 observed La Palma area at $64^{\circ}10'$ from Nadir, near the edge of the field of view (Table 3).

2.2.1 Advantages of GOES12 Satellite

We preferred to use GOES among the other satellite for several reasons that are explained below:

¹ See <http://archive.eso.org/asm/ambient-server>

Table 2. Total amount of consecutive nights covered by each databases.

Site	Ground Data	Satellite Data
Paranal	730	700
La Silla	730	700
La Palma	730	700
Mt. Graham		700
Tolonchar		700

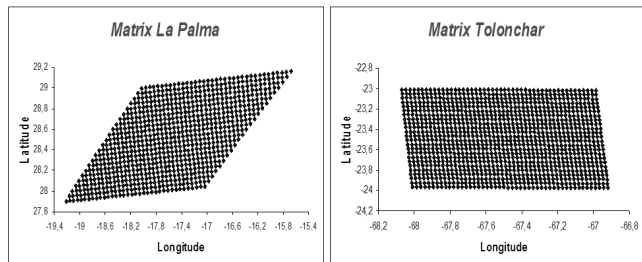


Figure 2. Comparison of one image matrix at La Palma and Tolonchar. The deformation is due to the satellite observation angle.

- Because it is possible to observe, with a single image, several sites simultaneously.
- Because, thanks to the very high orbit (35800km), the satellite is extremely stable and not affected by phenomena of high exosphere.
- Because, thanks to this set-up, it is possible to have the same instrumental configuration for each site and to compare them in a suitable way.
- Because GOES12 data have a high temporal resolution (41 sec as maximum value) and the complete day coverage.
- Because GOES12 observe the site at any time of the day. Instead polar satellites are bound to individual orbits. This allows to use an hourly analysis instead of a daily average of atmospheric conditions.
- Because GOES12 data have a high spatial resolution (1 km for visual to 4 km in IR bands).
- Because GOES12 provides five simultaneous images, one for each band, and it is the only satellite with the CO_2 band (13, $30\mu m$) very useful for the analysis of lower atmosphere phenomena.
- Because GOES12 have a long term database, useful for long time analysis.
- Because presents the same deterioration of images due to the inevitable degrade of the satellite. As a consequence the comparison between different sites is not influenced by the use of different instruments or different images.

3 SATELLITE DATA ACQUISITION

For the purposes of this work, we used GOES12 equipped with the imager. Among the 5 available channels, as shown in Table 1, we have selected the water vapor channel (channel 3, hereafter called B3 band) centered at $6.7\mu m$, the cloud coverage channel (channel 4, hereafter called B4 band) centered at $10.7\mu m$, and the CO_2 band (channel 6, hereafter

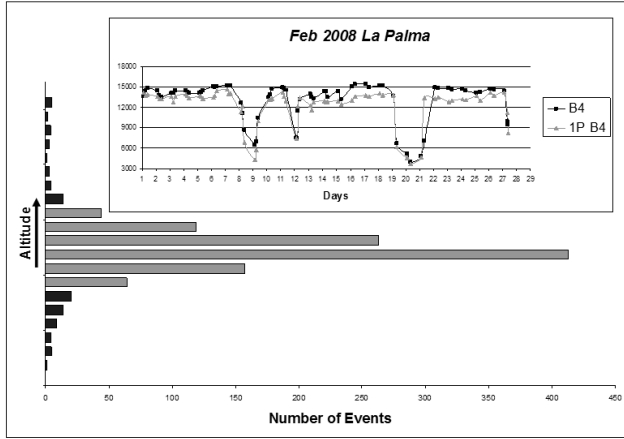


Figure 3. Correlation between the Matrix $1^\circ \times 1^\circ$ vs the single pixel. At La Palma in 2008 the histogram shows a correlation of 92%. The gray bars represent the data within the threshold $\leq |1\sigma|$, while black bars are the data with difference $> |1\sigma|$. The upper panel represents a pattern of $1^\circ \times 1^\circ$ matrix (black line) and the single pixel (gray line) in B4 band for a single month. The altitude corresponding to the peak of the histogram corresponds to about 4000m as indicated by the B4 weighting function of GOES12 satellite (**Bin**= 250m). We note that the main differences arise from low-altitude phenomena.

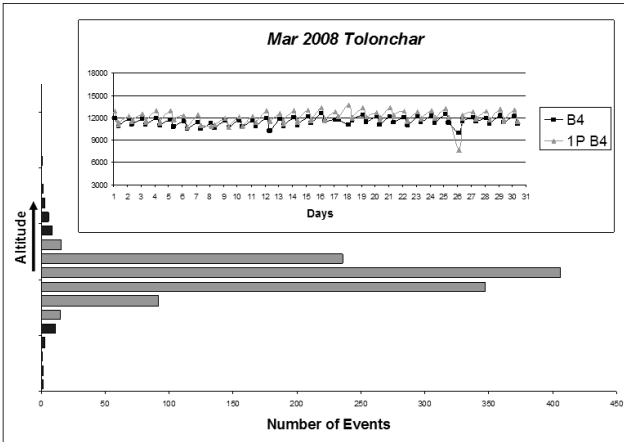


Figure 4. Correlation between the Matrix $1^\circ \times 1^\circ$ vs the single pixel. At Tolonchar in 2008 the histogram shows a correlation of 96%. The gray bars represent the data within the threshold $\leq |1\sigma|$, while black bars the data with difference $> |1\sigma|$ (**Bin**= 250m). The upper panel represents a pattern of $1^\circ \times 1^\circ$ matrix (black line) and the single pixel (gray line) in B4 band for a single month.

called B6 band) centered at $13.3 \mu\text{m}$. B3 band is sensitive between $6.5 - 7.0 \mu\text{m}$ and is able to detect high altitude cirrus clouds, B4 band is sensitive between $10.2 - 11.2 \mu\text{m}$ and is able to detect middle level clouds, while B6 band is able to sense small particle such as fog, ash and semi-transparent high clouds. Data are a measurements of thermal radiation emitted during the night. The selection of the IR channels was done in order to detect clouds at different heights, because water vapor absorbs electromagnetic radiation and then re-emits it in various wavelength bands, in

Table 3. Geographic characteristics of the analyzed sites and GOES12 satellite. The view angle is obtained through the formula $\theta = \sqrt{(\Delta\text{LAT})^2 + (\Delta\text{LONG})^2}$.

site	LAT.	LONG.	Altitude Km	View Angle
Paranal	$-24^\circ 37'$	$-70^\circ 24'$	2.630	$25^\circ 00'$
La Silla	$-29^\circ 15'$	$-70^\circ 43'$	2.347	$29^\circ 30'$
La Palma	$+28^\circ 45'$	$-17^\circ 52'$	2.363	$64^\circ 10'$
Mt. Graham	$+32^\circ 42'$	$-109^\circ 52'$	3.267	$47^\circ 40'$
Tolonchar	$-23^\circ 56'$	$-67^\circ 58'$	4.480	$24^\circ 50'$
GOES12	$+0^\circ 00'$	$-75^\circ 00'$	35800	

particular in the infrared region at $6 - 7 \mu\text{m}$. If clouds are not present, the emissions at $10.7 \mu\text{m}$ reaching the satellite is largely not absorbed by the atmosphere so the measured radiance values are due to emission from surface. Instead when clouds are present, the emissivity drops. Data are prepared by the Comprehensive Large Array-data Stewardship System (CLASS), an electronic library of NOAA environmental data², and are stored as rectified full earth disk images in a format called AREA files. We processed them using McIDAS-V Version 1.0beta4, a free ware software package. First we extracted the GOES data on the telescope sites.

Table 3 shows the geographic coordinates of the analysed sites. For each site we have identified and extracted a sub-image of $1^\circ \times 1^\circ$ having the central pixel centered on (or near) the coordinates given in Table 3.

Due to the discrete grid of the available GOES data the distances from the central pixel for each site are: $5' \pm 1'$ at Paranal, $6' \pm 1'$ at La Silla, $5' \pm 1'$ at La Palma, $3' \pm 1'$ at Mt. Graham and $4' \pm 1'$ at Tolonchar. These distances are very small compared to the used matrix.

For each night we have extracted the observations at three different hours: at 02:45, 05:45, 8:45 because they are the local times in common for all sites under investigation available from GOES12 satellite. In case of not availability of the specific images, the nearest temporal image was used. The last column of Table 3 shows the satellite view angle. Figure ?? shows the two different projections obtained from each acquisition at La Palma and Tolonchar.

In Paper III the analysis of the amount of clear sky fraction at La Palma and Mt. Graham was based following the same approach of Erasmus & van Rooyen (2006). We have used the B3 and B4 bands separately to sense thick clouds, but the old procedure presented some limits in case of partial coverage or thin clouds. In this paper we refine the analysis using a new and more sophisticated channel correlation analysis in order to detect more subtle effects due to atmospheric perturbations, including sudden changes in air masses, which imply changes in seeing, wind and relative humidity. We also included in the analysis the B6 band, see Section 5. We believe that these previous limits are overcome by correlating B4 with B3 and B6 bands. Another difference in this new analysis is that the flux is averaged on an area of $1^\circ \times 1^\circ$ instead the 1 pixel value obtaining significant decrease of the instrumental noise. A comparison

² www.class.ngdc.noaa.gov

of the two procedures is described in the following section. This matrix analysis is validated using the GOES 12 data of La Palma and Tolonchar because the two sites show very different geophysical conditions and different satellite angle of view. After the positive validation we decided to extend the same analysis to Paranal, La Silla, and Mt.Graham.

3.1 Resolution Correlation Matrix

The histograms of Figures 3 and 4 show the correlation between the Matrix $1^\circ \times 1^\circ$ vs the single pixel at La Palma and Tolonchar in the year 2008 for B4 band. Section 7.1 describes the selected threshold used in this classification.

The grey bar of each histogram represents the data with absolute value $\leq |1\sigma|$ level, black bars show data $> |1\sigma|$ level. Moreover the histogram represents the distribution of the B4 band in altitude. The peak of the histogram corresponds to about 4000m at La Palma, and greater than 4000m at Tolonchar, see Section 4.1.

The altitude was extrapolated from the B4 weighting function of GOES12 satellite. The peaks of these functions at high altitude and the use of matrix make the model suitable and sensitive for the study of atmospheric layers above the telescope sites. In particular, clouds below the level of the observing site do not affect the model as demonstrated by the high correlation percentage.

In fact the 92% of data at La Palma are within $|1\sigma|$ level, the 96% at Tolonchar. The inset plots of the Figures 3 and 4 represent the correlation of B4 flux computed as a mean value in a $1^\circ \times 1^\circ$ matrix (black line), and B4 flux obtained in a single pixel (grey line) for March 2008 at Tolonchar and February 2008 at La Palma. February is chosen as a typical perturbed month because of the wide count fluctuations. In each case we see that the mean matrix and 1 pixel values show a similar pattern, this means that we are looking at a high altitude compared to the height site. For the figures we have chosen critical months to show that the correlation is good for any atmospheric condition and then of the season. We decide to use the matrix, instead the 1 pixel value, because the average of the flux gives more stable information reducing the fluctuations due to instrumental noise. A further advantage in the use of matrix is that we are looking at a wider field of view than in the one-pixel analysis.

We are confident that thanks to the high correlation we obtain statistical reliable data. As shown, the histogram is correlated with the altitude of the site, through the comparison between the matrix and the single pixel we can also extract information on the site analyzed.

La Palma histogram clearly shows an asymmetric distribution showing that perturbations are mainly due to low altitude. A check we done to confirm this point extracting the log comments of data located on the low side of the histogram queue. We found that the majority of the comments are "freezing fog" and data are from winter time.

At Tolonchar the distribution is symmetric and with an almost negligible queue.

4 REMOTE SOUNDING BASIC MODEL

The mathematical model used in this analysis is here explained. The emitted monochromatic radiation intensity at

a given λ and along a vertical path at the top of the atmosphere, incident at a satellite instrument is given by:

$$R_\lambda = (I_0)_\lambda \tau_\lambda(z_0) + \int_{z_0}^{\infty} B_\lambda T(z) K_\lambda(z) dz \quad (1)$$

where:

- $K_\lambda(z) = \frac{d\tau_\lambda(z)}{dz} \Rightarrow$ Weighting Function (WF)
- $B_\lambda T(z) \Rightarrow$ Planck function profile as function of vertical temperature profile T
- $(I_0)_\lambda \Rightarrow$ Emission from the earth surface at height z_0
- $\tau_\lambda(z) \Rightarrow$ Vertical transmittance from height z to space

This equation may also be extended to represent radiation emitted along a slant (non-vertical) path making the approximation of a plane-parallel atmosphere.

For a viewing path through the atmosphere at angle θ to the vertical, we have:

$$\tau_\lambda(z, \theta) = e^{-\sec\theta \int_z^{\infty} K_\lambda(z) c(z) \rho(z) dz} \quad (2)$$

where:

- $\rho(z) \Rightarrow$ Vertical Profiles of Atmospheric Density
- $K_\lambda(z) \Rightarrow$ Absorption Coefficient
- $c(z) \Rightarrow$ Absorbing Gas Mixing Ratio

Changing from the notation of a continuous profiles, as in equation (1), to discrete profile, and considering the atmosphere as a composition of many thin layers, the corresponding equation becomes:

$$R_i = (I_0)_i \tau_i(z_0) + \sum_{j=1}^{j-1} B_{ij} K_{ij} \quad (3)$$

Making substitutions as below:

- $B_j \Rightarrow I_0$
- $K_{ij} \Rightarrow \tau_i(z_0)$

Hence equation is given by

$$R_i = \sum_{j=1}^j B_j K_{ij} \quad (4)$$

Representing the radiance in all channels and the Planck function profile by vectors we have:

$$\vec{R} = \vec{B} \cdot \vec{K} \quad (5)$$

where \vec{K} is a matrix containing the discrete weighting function elements $i \times j$. Assuming the problem to be linear (i.e. \vec{K} is \vec{B} independent) the formula to find out the \vec{B} function can be inverted.

4.1 The Weighting Functions of GOES12

The weighting function (WF) specifies the layer from which the radiation emitted to space originates, and hence it determines the region of the atmosphere which can be sensed from space at fixed λ .

In such a way many atmospheric layers can be observed by selecting different λ values.

If a standard atmosphere is assumed GOES12 WFs have the following median height values³:

³ See <http://cimss.ssec.wisc.edu/>

- BAND3: $K_{\lambda_3}(z) = \frac{d\tau_{\lambda_3}(z)}{dz} \Rightarrow \approx 8000m$
- BAND4: $K_{\lambda_4}(z) = \frac{d\tau_{\lambda_4}(z)}{dz} \Rightarrow \approx 4000m$
- BAND6: $K_{\lambda_6}(z) = \frac{d\tau_{\lambda_6}(z)}{dz} \Rightarrow \approx 3000m$

These heights depend on the location of the selected earth region. For instance Tolonchar B3 height is supposed to be fairly constant while B4 and B6 heights are higher because the site is 4480m height. In any case experimental observations confirm that GOES12 B3-B4-B6 bands looks at high layers as regard to soil.

5 THE ANALYSIS OF THE INFRARED B3-B4-B6 GOES12 BANDS

A cloud cover analysis is possible by mean of Remote Sounding (RS) application to B3, B4 and B6: in the current models based mainly on B4 analysis only. This band fairly matches thick cloud observation, but it presents some limits in case of thin clouds or minor atmospheric events. These limits are mostly overcome by correlating this band with B3 and B6. Ground vs satellite data show that B3 is capable of detecting atmospheric events such as winds or relevant air displacements. Moreover different air mass changes (e.g. dry, wet, warm or cold wind) is detectable by comparing B4 to B3. Finally a correlation between B6 and B4 allows to gather information about fogs, dusts, thin clouds. In such a way remote sounding model applied to GOES12 bands provides the following atmospheric scheme:

- B3-B4 correlation: high atmospheric events and in particular air mass displacements.
- B4-B6 correlation: low atmospheric events, and in particular fogs, dusts, humidity.

On this base we can provide a sort of **atmospheric tomography** by satellite data extrapolation. Figure 5 shows the distribution of GOES12 emissivity in the three bands at Paranal (upper panel) and the distribution of correlation function $F_{C.A.}(t)$ (bottom left panel) for the month of September 2008. The corresponding atmospheric correlation function it is also shown in the right side of the panel. For each month we have obtained these distributions.

6 ATMOSPHERIC CORRELATION FUNCTION

As written in the previous sections the $F_{C.A.}(t)$ correlation function used in this analysis is based on three band correlation. Considering GOES 12 WFs the best Remote Sounding is:

$$I_{C.A.} = I_{\lambda_3} - [I_{\lambda_6} - I_{\lambda_4}] \quad (6)$$

This model takes into account auto-corrections of atmosphere: for instance if two high layers have a positive oscillation and lower layers has an equal magnitude oscillation, but negative, the $F_{C.A.}(t)$ remains constant. From the physical point of view this means that the corresponding wave front observed from earth will be automatically corrected and an event is never been observed, as high atmosphere oscillations provoked by the B3-B4 correlation are always greater than those provoked by the B4-B6 correlation. B4-B6 oscillations

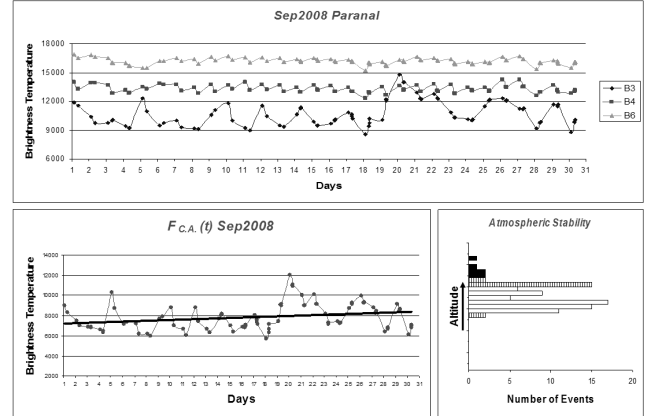


Figure 5. GOES 12 emissivity in B3, B4, B6 bands (upper panel) at Paranal for September 2008. Left panel shows the correlation function (the black straight line represents the $F_{C.A.}(t)$ trend-line). The corresponding atmospheric stability histogram is shown in the right lower panel.

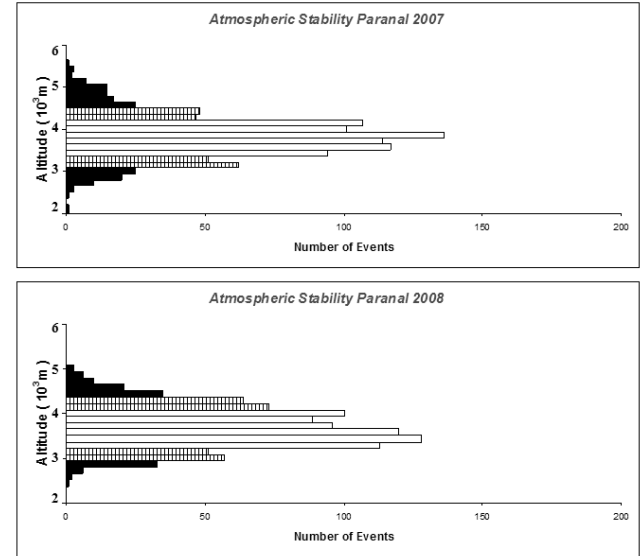


Figure 6. Histogram of annual atmospheric stability at Paranal. White bars represent the stable nights, gray bars clear but unstable nights, black bars the nights covered.

can only partially correct the wave front.

In mathematical terms this model provides a brightness temperature of the B3, B4 and B6 combination, given by equation:

$$I_{C.A.} = \frac{R_{\lambda_3} + R_{\lambda_4} - R_{\lambda_6}}{\tau(z_0)} + \frac{\int_{z_0}^{\infty} B_{\lambda_3}[T(z)]K_{\lambda_3} + B_{\lambda_4}[T(z)]K_{\lambda_4} - B_{\lambda_6}[T(z)]K_{\lambda_6} dz}{\tau(z_0)} \quad (7)$$

$F_{C.A.}(t)$ can be extrapolated by relating T brightness to time. This function will provide information about atmospheric quality of the surveyed site and the height of the perturbation that is a function of the T brightness. We show in Section 6.2 that this function is related to the seeing. Subsequently the air mass displacements (dynamical atmo-

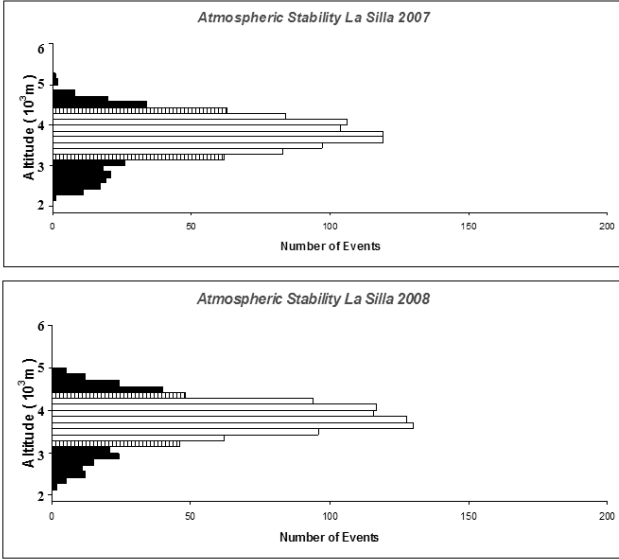


Figure 7. Histogram of annual atmospheric stability at La Silla. White bars represent the stable nights, gray bars clear nights but unstable, black bars the nights covered.

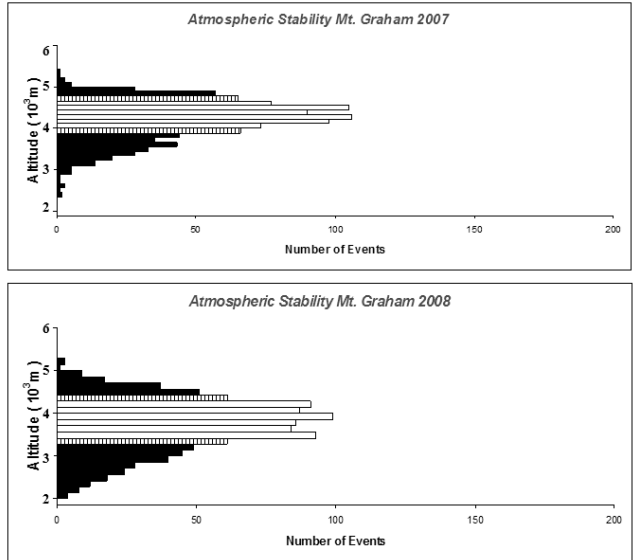


Figure 9. Histogram of annual atmospheric stability at Mt. Graham. White bars represent the stable nights, gray bars clear nights but unstable, black bars the nights covered.

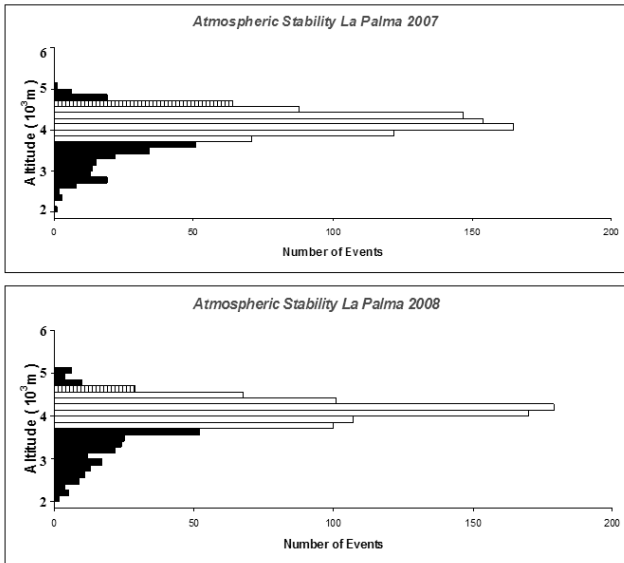


Figure 8. Histogram of annual atmospheric stability at La Palma. White bars represent the stable nights, gray bars clear nights but unstable, black bars the nights covered. We note that La Palma instability (black bars) is due mainly to low-altitude phenomena such as fog, dust, etc. as confirmed by log comments.

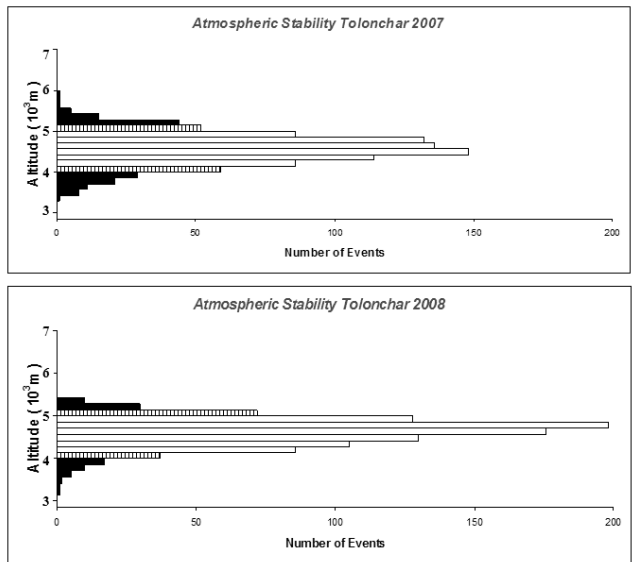


Figure 10. Histogram of annual atmospheric stability at Tolonchar. White bars represent the stable nights, gray bars clear nights but unstable, black bars the nights covered.

spheric instability) can be ranked according to their altitude and then to the kinetic energy. Figure 5 will represent a pattern of B3, B4 and B6 at Paranal. The bottom of Figure 5 shows the correlation function extrapolated through the RS and the respective histogram of atmospheric stability. This histogram also gives us information on the share that generates the disturbance. We note that the flat distribution of the B4 and B6 show no cloud cover, unlike that of B3, which has strong oscillations. Assuming a standard atmosphere for this band observed at a height of $\approx 8000m$, we

infer that the phenomena are of high altitude. Observations from the ground confirm the presence of strong winds and a worsening of the seeing. Figures 6, 7, 8, 9, 10 depict the histogram of annual atmospheric stability. White bars represent the stable nights, gray bars clear nights but unstable, black bars the nights covered (see Section 7.1.3 for definitions). The thresholds were obtained solely from analysis of satellite data. Histograms were derived from the correlation function, so they can give information on the contribution of atmospheric phenomenon in question.

6.1 Satellite Atmospheric Tomography

The atmospheric stability is derived from the atmospheric correlation function. This function, extrapolated from the RS of B3, B4 and B6 bands, is correlated to the integrated structural parameter of the refraction index (C_n^2) and than to the optical turbulence. In fact, as shown below, the RS of the B3, B4 and B6 bands is function of the changes in temperature at various altitudes. Atmospheric stability can be estimated by involving the model depicted below. Let's consider brightness temperature processed using **McIDAS-V** package. From a theoretical point of view the brighter a GOES12 image pixel the hotter the observed layer (i.e. lower layer).

Emitted radiation intensities at different satellite observation λ are then:

$$R_{\lambda_3} = (I_0)_{\lambda_3} \tau_{\lambda_3}(z_0) + \int_{z_0}^{\infty} B_{\lambda_3} T(z) K_{\lambda_3}(z) dz$$

$$R_{\lambda_4} = (I_0)_{\lambda_4} \tau_{\lambda_4}(z_0) + \int_{z_0}^{\infty} B_{\lambda_4} T(z) K_{\lambda_4}(z) dz$$

$$R_{\lambda_6} = (I_0)_{\lambda_6} \tau_{\lambda_6}(z_0) + \int_{z_0}^{\infty} B_{\lambda_6} T(z) K_{\lambda_6}(z) dz$$

These equations provide informations about layer height and temperature. Plotting these data as function of time an atmospheric instability function can be extrapolated.

6.2 Correspondence between the Seeing and the Atmospheric Correlation Function

In this section we detect a possible correlation between the seeing obtained from the web page of the Robotic Differential Image Motion Monitor (known as RoboDIMM⁴) of Isaac Newton Telescope (INT) and the atmospheric correlation function $FC.A.(t)$ computed for the la Palma sky to test a possible correlation with the image quality.

This RoboDIMM, like all classical DIMMs, relies on the method of differential image motion of telescope sub-apertures to calculate the seeing Fried parameter r_0 . RoboDIMM forms four separated images of the same star, and measures image motion in two orthogonal directions from which it derives four simultaneous and independent estimates of the seeing. The data interpretation makes use of the Sarazin and Roddier's DIMM algorithm as described in (Sarazin & Roddier (1990)), based on the Kolmogorov theory of atmospheric turbulence in the free atmosphere. There is the possibility that some DIMMs, including the RoboDIMM may have a lower limit threshold in the measurement of the seeing, due to noise, but in our sample (Figures 11, 12 and 13) the seeing values do not have values significantly below 1 arcsec . Moreover in this paper we do not intend to give an absolute calibration but only a correlation analysis of these two functions.

In fact the solid gray line represents the $FC.A.(t)$ trend. The discontinuous black line represents the available seeing values. We note that the seeing is worse if the $FC.A.(t) > |1\sigma|$ as referred in Section 7.1.3. A dedicated **Site Testing** can

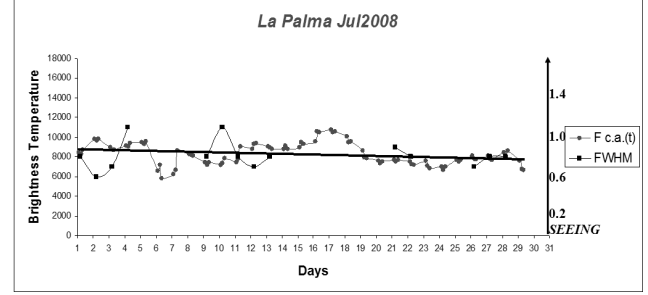


Figure 11. Atmospheric Correlation Function-FWHM Correspondence. La Palma, July 2008. The solid gray line represents $FC.A.(t)$ trend. The discontinuous black line represents the available seeing values. The black straight line represents the $FC.A.(t)$ trendline. We note that the worse seeing occurs when the MAX and min values of the $FC.A.(t)$ correspond (Correlation Coefficient= 0.92).

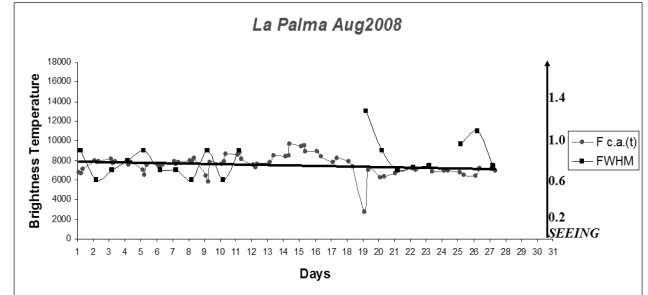


Figure 12. Atmospheric Correlation Function-FWHM Correspondence. La Palma, August 2008. The solid gray line represents $FC.A.(t)$ trend. The discontinuous black line represents the available seeing values. The black straight line represents the $FC.A.(t)$ trendline. We note that the worse seeing occurs when the MAX and min values of the $FC.A.(t)$ correspond (Correlation Coefficient= 0.91).

clearly improve current models, providing information about fundamental parameters. In a future paper we are planning, after an accurate set up of the ING's RoboDIMM (Isaac Newton Group of Telescopes), to correlate the values of seeing with the values of $FC.A.(t)$.

We specify that this is still a preliminary work. We plan in future to improve this model with the use of other seeing data bases and/or preferably $C_n^2(h)$ profiles.

7 TEMPORAL DATA ANALYSIS

The ground-satellite correlation model used in this article is based on a temporal data correspondence of ≈ 3 values for each night. We have in fact multiple values for each night (≈ 3) and this gives us the opportunity to do a detailed analysis of various conditions. We have also a larger number of data and this, from a statistical point of view, allows to validate the model.

Figure 14 and 15 shown the plots of the obtained temporal emissivity of B4 band vs B6 for the 2008 at Paranal and at La Palma. The nights are classified as a function of the sky quality obtained from the observing log of each analysed site. It appears that clear nights present high values of

⁴ See <http://catsserver.ing.iac.es/roboDIMM/>

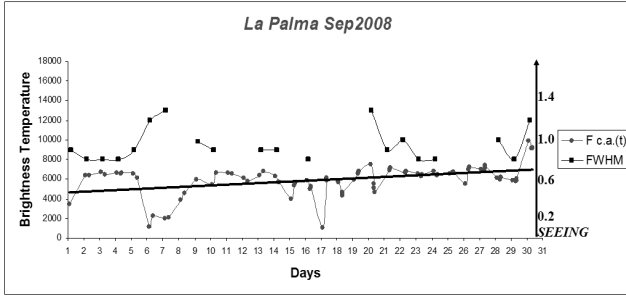


Figure 13. Atmospheric Correlation Function-FWHM Correspondence. La Palma, September 2008. The solid gray line represents $F_{C.A.}(t)$ trend. The discontinuous black line represents the available seeing values. The black straight line represents the $F_{C.A.}(t)$ trendline. We note that the worse seeing occurs when the MAX and min values of the $F_{C.A.}(t)$ correspond (Correlation Coefficient=0.88).

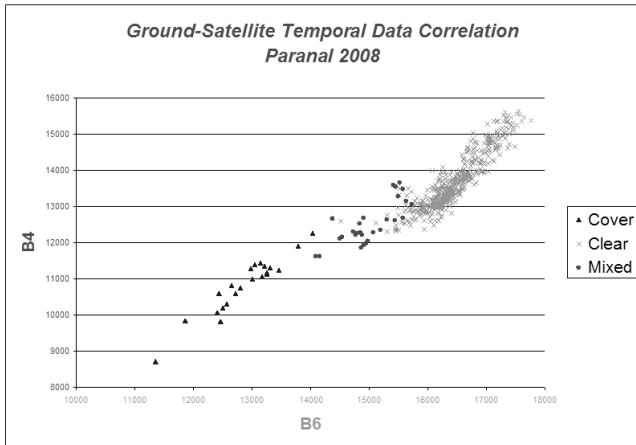


Figure 14. Temporal distribution of GOES12 B4 and B6 band emissivity at Paranal in 2008. Sky quality classification has been carried out using the Paranal log.

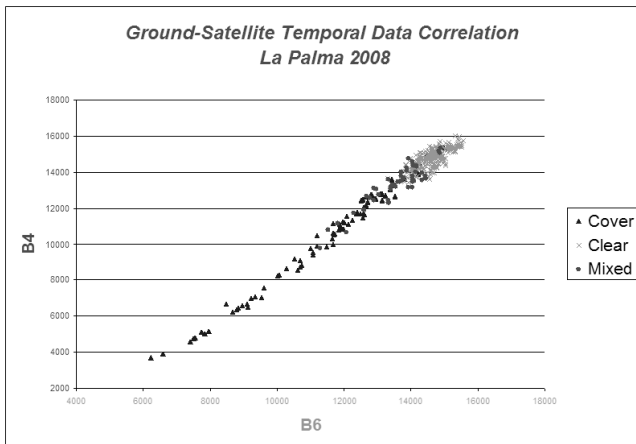


Figure 15. Temporal distribution of GOES12 B4 and B6 band emissivity at La Palma in 2008. Sky quality classification has been carried out using the merge of TNG and Liverpool ground based data.

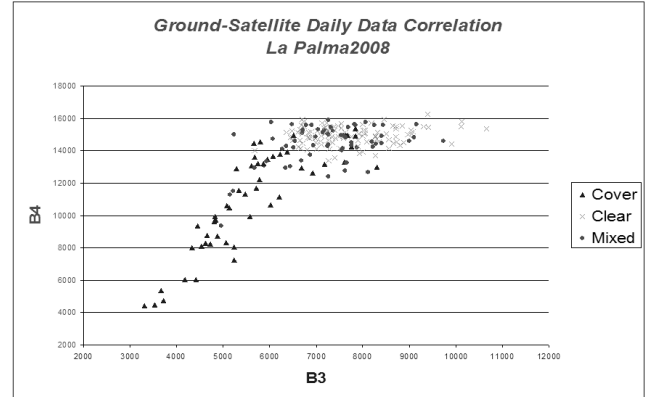


Figure 16. Daily distribution of GOES12 B3 and B4 band emissivity at La Palma in 2008. Sky quality classification has been carried out using the TNG log.

emissivity.

Moreover Fig. 15 shows a lower dispersion and a better separation of clear nights if compared with Fig. 16 confirming once more the better quality of the adopted method. From Fig. 14 and Fig. 15 we can define as clear all the nights having $B4 \geq 13000$ Units at Paranal, while at La Palma we can define as clear all the nights having $B4 \geq 13900$ Units. Table 4 shows the obtained percentage of clear, mixed and covered nights at Paranal and at La Palma in the year 2008 from a temporal punctual analysis. As in Paper III, we have found that the fractions of clear time based on satellite data are greater than those of clear nights using ground based data. The differences seem higher than the biases of single logbooks. In fact the amount of nights computed using the different adopted logbooks gives a similar percentage with differences around 2% (computed in the same period, 2008-2009) when a careful and homogeneous analysis is performed.

The obtained percentages are in reasonable agreement with the results reported in Garcia-Gil et al. (2010).

We can conclude that the nights classification is more dependent on the adopted methodology and accuracy rather than on biases in the adopted logbooks. The differences can be better explained considering that some local effects could be ignored by satellites. In addition, we note that considering the fraction of clear time fraction from satellite data vs. that of clear nights from ground data, the first fraction is obviously higher.

However we don't expect a large discrepancy as we demonstrated in Paper III where we found that the fraction of partially used nights is very small. It is interesting to note that we found an amount of satellite clear nights close to that obtained in Paper III even if we have used different bands: we obtained 71.9% of clear nights in Paper III, obtained analysing B3 vs B4 bands, and 71% of clear nights in the present analysis obtained plotting B4 vs B6 bands, but the thresholds are fixed considering only B4 (see Section 7.1.2).

The last row of Table 4 shows the percentage of accuracy to associate to each obtained fraction of nights. The uncertainty is computed as follows:

$$\bullet \Delta_{Clear/Mixed} \Rightarrow \text{Clear/Mixed Uncertainty}$$

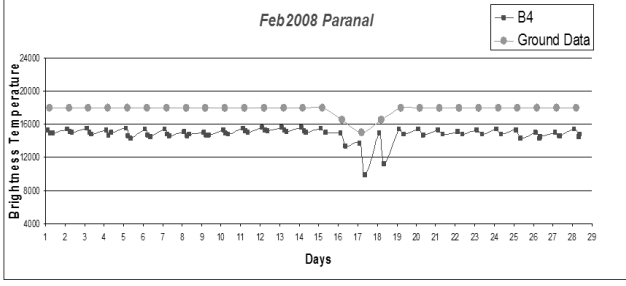


Figure 17. Ground Data-Satellite Data Correlation. Paranal, February 2008.

- $\Delta_{Clear/Covered} \Rightarrow$ Clear/Covered Uncertainty
- $\Delta_{Mixed/Covered} \Rightarrow$ Mixed/Covered Uncertainty

We note that the largest satellite uncertainty derives from the overlap of clear and mixed nights, while the satellite is accurate in other cases. It is interesting the comparison between the temporal and daily methods.

Figure 16 represents daily distribution of GOES12 B3 and B4 band emissivity at La Palma in 2008. We note how the graph is more dispersed compared to the graph of Figure 15. This is due to the greater accuracy of the temporal method and the use of different bands: B3 and B6 respectively. In fact the B6 trend is more regular.

Table 5 shows the comparison between temporal and daily data analysis. We can observe how the temporal method uncertainties are smaller than the daily method uncertainties. In this case we chose annual thresholds and considered the mathematical error, the method provides the greatest advantages choosing monthly thresholds and considering the statistical error. The monthly thresholds make it possible to consider seasonal temperature changes of the site reducing the overlap percentages.

As final check Figure 17 plots the B4 emissivity (black line) and log ground data (gray line) for February 2008 at Paranal. It is evident that the monthly distribution of the emissivity follows the ground data.

7.1 Discussion of Error Propagation and Thresholds

In our model the various thresholds to classify the nights were chosen by the individual analysis of satellite data. This also allows to study sites for which we have no ground data. The thresholds were selected via the night temperature range detected by satellite and not through the real night brightness temperature range of the site.

This choice was made because the satellite temperature resolution decreases with the observation angle. In fact at La Palma we observe a temperature range lower than other sites. If we consider:

$$\text{Night Satellite Temperature Range} = 1\sigma$$

we note that the use of the matrix decreases the threshold value reducing the satellite noise. This makes the model more accurate (Fig.18).

The thresholds for each data classification are described below.

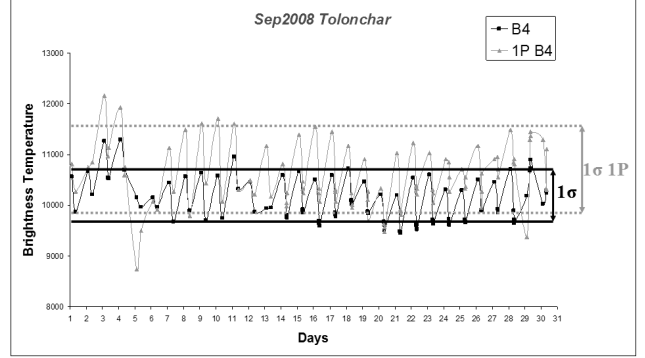


Figure 18. Comparison between the single pixel threshold of 1σ and the matrix threshold of 1σ at Tolonchar in September 2008. Figure represents a pattern of $1^\circ \times 1^\circ$ matrix (black line) and the single pixel (gray line) in B4 band for a single month. We note how the use of the matrix decreases the threshold value reducing the satellite noise. This makes the model more accurate.

7.1.1 Resolution Correlation Matrix Thresholds

In this section we compare the brightness temperature difference between the single pixel and the matrix method. We assume that the data are correlated if the difference is $\leq |1\sigma|$. Figures 3 and 4 report the obtained percentage of correlation.

$$|T_{Brightness}^{1Pixel} - T_{Brightness}^{Matrix}| < |1\sigma|$$

where:

- $T_{Brightness}^{1Pixel} \Rightarrow$ Brightness temperature of the single pixel
- $T_{Brightness}^{Matrix} \Rightarrow$ Brightness temperature of the $1^\circ \times 1^\circ$ matrix

7.1.2 Clear, Mixed, Covered Nights Classification

The nights are classified using GOES12 B4 band. The classification of the nights is based in the following assumption: the maximum monthly brightness temperature T_B^{Max} occurs in clear condition.

The other monthly brightness temperatures are correlated with T_B^{Max} when:

- $T_B^{Max} - T_B \leq 2\sigma \Rightarrow$ Clear
- $2\sigma < T_B^{Max} - T_B \leq 3\sigma \Rightarrow$ Mixed
- $T_B^{Max} - T_B > 3\sigma \Rightarrow$ Covered

where $T_B \Rightarrow$ Brightness temperature of the $1^\circ \times 1^\circ$ matrix.

From this definition "clear" sky means a matrix where there are no clouds. As concerning the ground based data we define "clear" the nights cloud free in the logbooks and completely usable for observations.

"Mixed" are nights where comments of presence of clouds or meteorological events (fog, wind, humidity...) have been found, but part of night was used.

"Covered" are unusable nights due to clouds or fog.

Table 4. Clear/Mixed/Covered nights percentage and overlaps at Paranal and La Palma in 2008. Temporal data analysis.

	Clear	Ground Mixed	Covered	Clear	Satellite Mixed	Covered
Paranal	91%	7%	2%	84%	14%	2%
La Palma	66%	12%	22%	71%	11%	18%
	Paranal			La Palma		
Uncertainty	$\Delta_{Clear/Mixed}$	$\Delta_{Clear/Covered}$	$\Delta_{Mixed/Covered}$	$\Delta_{Clear/Mixed}$	$\Delta_{Clear/Covered}$	$\Delta_{Mixed/Covered}$
Percentage	7%	1%	2%	7%	3%	5%

Table 5. Clear/Mixed/Covered nights percentage and overlaps at La Palma in 2008. Comparison between temporal and daily data analysis.

	Clear	Ground Mixed	Covered	Clear	Satellite Mixed	Covered
La Palma (Daily)	60%	21%	19%	69%	15%	16%
La Palma (Temporal)	66%	12%	22%	71%	11%	18%
	La Palma (Daily)			La Palma (Temporal)		
Uncertainty	$\Delta_{Clear/Mixed}^D$	$\Delta_{Clear/Cover}^D$	$\Delta_{Mixed/Cover}^D$	$\Delta_{Clear/Mixed}^T$	$\Delta_{Clear/Cover}^T$	$\Delta_{Mixed/Cover}^T$
Percentage	9%	3%	9%	7%	3%	5%

7.1.3 Clear, Stable Nights Classification

We calculated the monthly percentage of clear time relying on temporal data analysis. With this method we classify the fraction of each night by reading multiple data (e.g. if we have three data for a night, two clear values and one covered value, the percentage of clear night will be 67%). This is a definition close to the classical "spectroscopic time". We define "stable" a clear sky without atmospheric phenomena that may affect the photometric quality (wind, fog, humidity).

The monthly percentage of photometric time is calculated by the same method and this is close to the classical definition of the "photometric time". This classification is very important because the photometric quality of clear sky, is influenced by phenomena not detectable by the methods currently used.

Finally, we clarify that an unstable sky might be still useful for observing because it is a subset of clear sky. This explains the differences in percentages of our classification (see Tables 6 and 7).

To be more clear we specify that we calculated the time fraction, not the whole night fraction.

If we take into account the atmospheric correlation function T_B^{Max} , it is possible to introduce the concept of stable nights. Considering $F_{C.A.}(t)$ trendline we get the following classification:

- $|T_B - T_B^{Trendline}| \leq |1\sigma| \Rightarrow$ Stable
- $|1\sigma| < |T_B - T_B^{Trendline}| \leq |2\sigma| \Rightarrow$ Clear
- $|T_B - T_B^{Trendline}| > |2\sigma| \Rightarrow$ Covered

where:

- (i) $T_B^{Trendline} \Rightarrow$ Brightness temperature of the monthly trendline
- (ii) $T_B \Rightarrow$ Brightness temperature of the $1^\circ \times 1^\circ$ matrix

Through this classification we obtain the histograms in Figures 6, 7, 8, 9, 10. White bars represent the stable nights, gray bars represent clear but unstable nights, black bars represent the covered nights.

The thresholds were obtained only from analysis of satellite data. Histograms were derived from the correlation function, so they can give information on the contribution of atmospheric phenomenon. The final results are reported in Tables 6 and 7.

7.1.4 Mathematics Errors Propagation

Tables 4, 5 show the uncertainties to associate to each single data computed through the formula:

$$\Delta_{Tot} = \sqrt{(\Delta_{Cl/Mix})^2 + (\Delta_{Cl/Co})^2 + (\Delta_{Mix/Co})^2}$$

obtaining the following values:

- Paranal $\Rightarrow \Delta_{Total} = 7.3\%$
- La Palma (Temporal) $\Rightarrow \Delta_{Total} = 9.1\%$
- La Palma (Daily) $\Rightarrow \Delta_{Total} = 13.1\%$

We observe that the temporal method for La Palma reduces the total uncertainty by 4%.

7.1.5 Statistics Errors Propagation

Now we consider the statistical error with the unbiased data assumption. We have $N(Ground; Satellite)$ pairs of values and in this case, considering the mathematical error for each site, the standard deviation on the function $F_\Delta(Ground; Satellite)$ is derived by the formula:

$$\sigma_{F_\Delta} = [\Delta_{Total}]^2$$

Finally, if we consider the number of data ($N(Ground; Satellite)$), the annual statistical uncertainty ($\Delta_{Statistical}$) of the model is given by the formula:

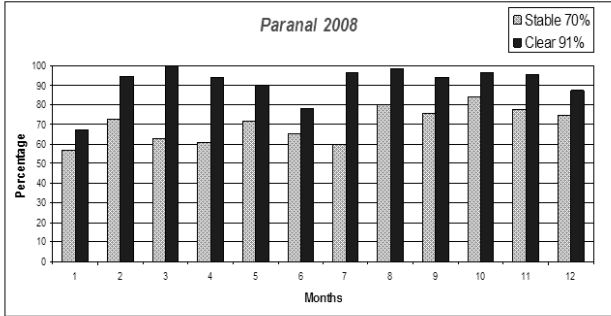


Figure 19. Clear and stable night fractions at Paranal 2008 from GOES12 satellite.

Table 8. Mathematical and statistical uncertainties of the model in 2008 at Paranal and La Palma.

Site	Δ_{Total}	$N(G; S)$	$\Delta_{Statistical}$
Paranal	7.3%	1050	2.0%
La Palma (Temporal)	9.1%	1020	3.0%
La Palma (Daily)	13.1%	340	9.0%

$$\Delta_{Statistical} = \frac{\sigma_{F\Delta}}{\sqrt{N(G; S)}}$$

Table 8 shows the obtained values whit the $\Delta_{Statistical}$ rounded to integers.

8 CONCLUSION

In this paper we have presented a new homogeneous method in order to obtain the amount of available time fraction. The data are extracted from GOES12 satellite imager on five very important and different astronomical sites in order to get comparable statistics. Satellite data are compared with ground based data.

In this analysis a wider spatial field is used in order to reduce the spatial noise: each value is the mean of $1^\circ \times 1^\circ$ matrix. The cloud coverage is obtained using GOES12 B4 and B6 bands independently. Using the correlation of three bands (B3, B4 and B6) we have computed an atmospheric correlation function as a further selection of the clear nights, and we have introduced the new concept of stable night. Temporal data are used for the years 2007 and 2008. We have shown that the derived atmospheric correlation function is correlated with the quality of the night in terms of FWHM (possibly also with wind and humidity). An example of clear/stable nights is given in Fig. 19 that shows the monthly distribution of 2008 nights at Paranal. The black bars represent the monthly percentage of clear nights, while the gray bars the percentages of stable nights. We can assume that stable nights could be the best approximation to the photometric nights. We obtained that the amount of stable nights is considerably lower than the clear nights in all the five analysed sites. In view of a better tuning of the stable nights as a function of the ground based parameters, we can adopt as a best approximation of the "clear nights" of the ground based log the satellite clear night percentages.

The mean of the 2007-2008 give a percentage of clear time of 88% at Paranal, 76% at La Silla, 72.5% at La Palma, 59% at Mt. Graham and 86.5% at Tolonchar. These percentage differences are higher than the statistical errors (Table 8).

Tolonchar and Paranal (Tables 6 and 7) show the largest number of clear nights but Tolonchar shows the largest number of stable nights, while La Palma shows that if a night is clear is also almost stable. Tolonchar appears the best site as concerning the stable nights while Paranal is the best for the clear nights (see also Figures 6 and 10).

The procedure adopted in this paper gives different percentages of satellite clear nights when compared with those of Erasmus & van Rooyen (2006). In fact we found 88% of clear nights at Paranal to compare with the Erasmus's percentage of 85%, instead, at La Palma we found the 72.5% to compare with the 83.7% of Erasmus. As already explained in the text the two methods differ mainly because (1) we use the direct brightness values of the satellite while Erasmus & van Rooyen (2006) converted them into temperatures and interpreted the absolute values of the temperatures in terms of height of the infrared emission, using a temperature-height sounding, and then of cloud coverage, and (2) they used a much smaller matrix. The authors pointed out that this technique has some limitations due to a number of effects, for example anomalous trends in temperatures during the night or for some types of clouds (monsoon clouds are an example). While their approach is certainly valid in terms of general physical interpretation, we found more direct and more reliable to work directly in terms of brightness relative time fluctuations. A deep analysis should be done comparing the results night by night but this is out of the scope of the present paper.

On the other hand we should take into account possible biases due to our time sampling, because we are measuring the second part of the night only. Our limit was set by the time availability of the Paranal ground log. In particular, phenomena that occurred during the first part of the night were not analyzed in this paper.

In addition we note that some low level phenomena could be missing (for example local dust clouds, fog...). A further possible bias is due to the satellite spatial resolution, mainly in sites with abrupt topography.

The use of higher resolution satellites, for example the MERIS spectrograph (on board of Envisat) with a spatial resolution of about 1 km, in principle should be better in these cases. Some authors obtained interesting results. For example Kurlandczyk and Sarazin (2007) used MERIS at La Silla and Paranal to get cloud coverage and precipitable water vapour and discussed the horography effects. However, in spite of its high spatial resolution MERIS presents some disadvantages compared to GOES. First the temporal coverage is much lower, second, MERIS is working in daytime and it does not give data during the night. As a consequence it can be used as a complement of GOES data to investigate the effects of spatial resolution, but its generalized use should be carefully validated site by site.

Finally, it is interesting to note the percentage differences between the two years, particularly at Mt. Graham, in 2008, the clear and stable nights percentage was considerably higher. We note minor differences also in the other sites. These could be a result of the El Niño phenomenon and its consequences at different sites.

Table 6. Satellite Mean Monthly Percentage 2007.

	Paranal		La Silla		La Palma		Mt.Graham		Tolonchar	
	Clear	Stable	Clear	Stable	Clear	Stable	Clear	Stable	Clear	Stable
January	73	55	72	72	38	38	48	48	54	42
February	90	61	90	88	61	61	45	45	72	62
March	86	65	75	75	52	52	51	51	81	63
April	74	58	64	58	75	75	61	61	94	64
May	91	72	59	59	86	86	59	59	87	87
June	60	55	33	33	94	88	72	72	69	69
July	89	82	56	56	93	86	14	14	82	82
August	87	76	65	65	93	93	41	41	89	89
September	94	78	73	73	80	80	44	44	100	92
October	100	91	93	90	80	80	72	69	93	84
November	98	80	85	85	48	48	53	52	93	79
December	80	55	78	78	84	80	72	71	91	76
Mean	85	69	70	69	74	72	53	52	84	74
Clear-Stable Mean	77		70		73		52		79	

Table 7. Satellite Mean Monthly Percentage 2008.

	Paranal		La Silla		La Palma		Mt.Graham		Tolonchar	
	Clear	Stable	Clear	Stable	Clear	Stable	Clear	Stable	Clear	Stable
January	67	57	100	68	52	52	49	49	52	52
February	95	73	96	74	68	68	60	60	85	81
March	100	63	93	74	52	52	86	80	99	74
April	94	61	82	82	77	77	93	78	100	80
May	90	72	71	71	87	82	75	70	91	77
June	78	65	64	64	90	90	74	66	72	72
July	97	60	74	65	95	84	20	20	99	88
August	99	80	72	72	90	90	24	24	95	91
September	94	76	56	56	71	71	74	74	100	97
October	97	85	80	77	82	82	86	80	100	89
November	96	78	97	88	37	37	71	71	100	83
December	88	75	100	85	45	45	62	62	70	70
Mean	91	70	82	73	71	69	65	61	89	80
Clear-Stable Mean	81		78		70		63		84	

It is possible to reduce the uncertainty of this methodology using all the available GOES12 IR bands and refining the tuning of the model. We found that using the correlation function from IR satellite data, it is also possible to observe several atmospheric phenomena (i.e. strong winds, damp winds, warm winds, fogs, humidity, dust etc).

A second paper on this correlation analysis is in progress to study of the cyclical fluctuations of this function to test the possibility to have a sort of now-casting seeing.

The possible synergy of this model with seeing forecast models may predict the atmospheric changes in the short and long time-scale, allowing the atmospheric conditions for science cases in order to have the best scientific results.

8.1 ACKNOWLEDGMENTS

The authors acknowledge dr.Vincenzo Testa, from National Institute for Astrophysics, Roland Gredel, from Heidelberg Max Planck Institute for Astronomy, Antonia M. Varela, from Instituto de Astrofísica de Canarias, Antonio Magazzu

from TNG and the former TNG Director Ernesto Oliva for the collaboration.

This activity is supported by the European Community (Framework Programme 7, Preparing for the construction of the European Extremely Large Telescope, Grant Agreement Number 211257) and by Strategic University of Padova funding by title "QUANTUM FUTURE".

Most of data of this paper are based on the CLASS (Comprehensive Large Array-data Stewardship System).

CLASS is an electronic library of NOAA environmental data.

This web site provides capabilities for finding and obtaining those data, particularly NOAA's Geostationary Operational Environmental Satellite data.

Finally we acknowledge the Liverpool Telescope website staff.

8.2 List of Acronyms

- GOES: Geostationary Operational Environmental Satellite
- MERIS: Medium Resolution Imaging Spectrometer
- CLASS: Comprehensive Large Array-data Stewardship System
- ESO: European Southern Observatory
- TNG: Telescopio Nazionale Galileo
- TMT: Thirty Meter Telescope
- INT: Isaac Newton Telescope
- ING: Isaac Newton Group of Telescopes
- DIMM: Differential Image Motion Monitor
- RoboDIMM: Robotic Differential Image Motion Monitor

REFERENCES

- Della Valle, A., Maruccia, Y., Ortolani, S., and Zitelli, V., 2010, MNRAS, 401, 1904 (Paper III)
- Erasmus, D., van Rooyen, R., 2006, in Stepp, L.M. Ed., Proc. of SPIE Vol. 6267, Ground-based and Airborne Telescopes.
- Lombardi, G., Zitelli, V., Ortolani, S., Pedani, M. J., 2006, PASP, 118, 1198 (Paper I)
- Lombardi, G., Zitelli, V., Ortolani, S., Pedani, M., 2007, PASP, 119, 292 (Paper II)
- Sarazin, M., Roddier, F., 1990, A&A, 227, 294-300
- Varela, A.M., Bertolin, C., Munoz-Tunon, C., Ortolani, S., and Fuensalida, J., J., 2008, MNRAS, 391, 507-520.
- Kurlandczyk, H., and Sarazin, M., 2007, proc. of SPIE vol. 6745, Remote Sensing of Clouds and the Atmosphere.
- Garcia-Gil, A., Muñoz-Tun, C., Varela, A.M., 2010, PASP 122, 1109-1121, Atmosphere Extinction at the ORM on La Palma: A 20 yr Statistical Database Gathered at the Carlsberg Meridian Telescope.